Resonant Commutation Electronic-Embedded DC Transformer (RC-EET DCX) with Quasi-Trapezoidal Current and Natural Current Sharing

Yuliang Cao, *Student Member*, *IEEE*, Khai Ngo, *Fellow*, *IEEE*, Dong Dong, *Senior Member*, *IEEE*

***Abstract* – High-power and high-density dc transformers (DCXs) are critical components in data center power supplies, energy storage systems, medium-voltage solid-state transformers, and transportation electrification. The challenges associated with designing high-power and high-frequency transformers are considerable. The electronic-embedded transformer (EET) concept, proposed in [1], is a response to these challenges, integrating semiconductor electronics into the transformer windings.**

In light of this concept, this paper presents two significant modifications. First, it replaces the complete full bridge with a low voltage bidirectional ac switch. Second, it introduces a resonant commutation (RC) to realize a quasi-trapezoidal transformer current with a smaller rms value. Compared to the triangular current produced by the original EET-DCX in [1], the rms current can be decreased by 15%.

In addition to streamlining the circuit, the proposed RC EET-DCX retains all the advantages of the original EET-DCX, including simple open-loop control and natural current sharing. By incorporating only one embedded bidirectional ac switch, the impedance of the high-frequency transformer leakage inductance is fully neutralized. As a result, the rated power of the proposed RC EET-DCX can be readily scaled up through transformer-level parallelism. Furthermore, the RC EET-DCX maintains the benefits of typical LLC/CLLC-DCX, including load-independent voltage gain, full load range zero voltage switching (ZVS), and low circulating current. To verify aforementioned benefits, a 12 kW RC EET-DCX with four planar RC EET units was built and tested.

***Index Terms* – High-power and high-frequency transformer design, zero voltage switching (ZVS), resonant commutation (RC), electronic-embedded transformer (EET), natural current sharing, dc transformer (DCX), bidirectional dc/dc converter.**

I. Introduction

To meet the demand of electrical vehicle (EV) charging systems [1]-[5], energy storage systems (ESS) [6]-[9], data center power supplies [7]-[9], and solid-state transformer (SST) systems [10]-[15], bidirectional fixed-ratio dc-dc converters, commonly known as dc transformers (DCXs), have been widely utilized. The DCX is highly efficient at bridging two dc buses due to its simple control, fixed switching frequency, and galvanic isolation. The front-end ac/dc stage [10]-[12], rear-end dc/dc stage [5]-[9], or an input-parallel-output-series (IPOS) dc regulator [7]-[12] can be adopted when the output voltage has a large variation range.

The dual active bridge (DAB) converter [13]-[15] and the LLC resonant converter [16]-[18] are two prevalent topologies for the DCX applications. Compared with DAB converter, LLC resonant converter is more desirable because of the lower circulating current, and full load range zero voltage switching (ZVS). Notably, when the resonant LLC/CLLC converter operates at (or slightly below) the resonant frequency as an LLC/CLLC-DCX, it can provide a load-independent constant voltage gain without any closed-loop voltage control [17]. However, when a resonant converter operates as a DCX, it's crucial to minimize the leakage inductance of the high-frequency transformer. This is because a larger leakage inductance could lead to higher current ringing during deadtime and increased voltage stress on the resonant capacitor [19]-[20].

However, as for the single transformer in LLC-DCX, there is an inherent trade-off between the operation frequency and power rating [1]. And thus, transformer-level parallel solution in Fig. 1 can be adopted. Compared with the typical converter-level parallel solution, transformer-level parallel solution is more desirable because the single full rating power inverting/rectifying bridge enables a high-density integration and low costs due to a smaller number of gate-drivers and auxiliary components.

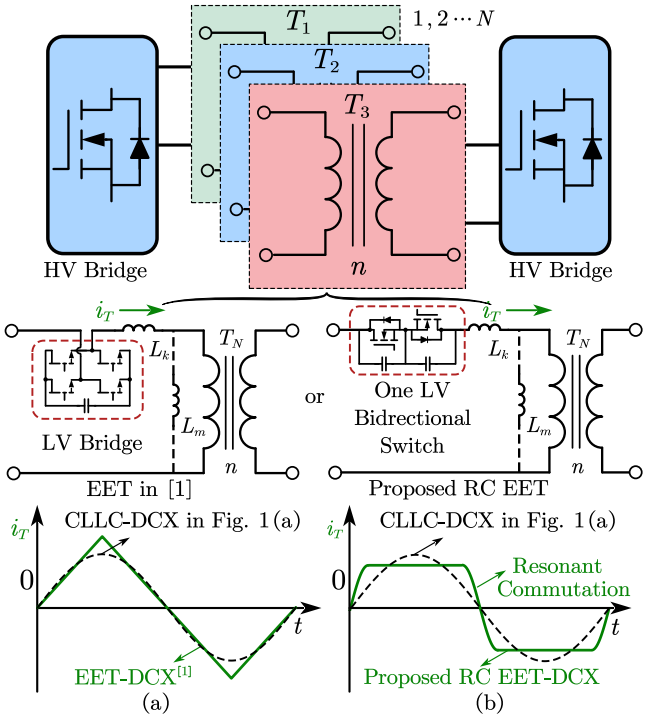

Fig. 1 Transformer-level parallel solution: (a) EET-DCX proposed in [1], (b) proposed resonant commutation (RC) EET-DCX.

However, with the typical LLC-DCX topology, the current sharing among paralleled high-frequency transformers is very sensitive to the resonant tank parameters because the current sharing is determined by the loop-impedance of each transformer, which is mainly determined by the total leakage inductance of each transformer in high-frequency range. As mentioned before, the leakage inductance of each high-frequency transformer is required to be minimized, any small inductance mismatch from manufacturing will lead to a significant current sharing mismatch. Even if there is a small parameter tolerance between two resonant tanks, the majority current will go through the tank with a smaller impedance, which might lead to poor efficiency and thermal issue.

To completely address the transformer-level parallel challenges in DCX application, a scalable electronic embedded transformer (EET) concept has been proposed in [1] to realizing the ultra-high-frequency, high-density, and high-power transformer design. As shown in Fig. 1(a), with the help of a very low-voltage (LV) full bridge integrated in each transformer, automatic current sharing can be achieved, and the total DCX rating power can be easily scaled up. After the combination of two high voltage (HV) full bridges as shown in Fig. 1, a scalable EET-DCX with several EET units was proposed in [1]. With a simple open-loop control for both HV and LV bridges, this scalable EET-DCX can provide a load-independent constant voltage gain with a natural current sharing among different EET units. Besides retaining LLC-DCX advantages such as full load range ZVS, the proposed EET-DCX has following additional merits: 1) Simple open-loop control; 2) Transformer-level parallel; 3) Natural current sharing; 4) Robust load-independent voltage gain; 5) Optimal operation at any frequency; 6) Scalability.

However, there are two remaining issues from EET-DCX:
1) Triangular transformer current without considering the magnetizing inductance. Compared with the sinusoidal current in traditional resonant CLLC-DCX, the triangular current depicted in Fig. 1(a) exhibits a larger root mean square (rms) value, which will cause higher conduction losses in both the devices and transformer windings.
2) Four extra active switches from LV bridge. As shown in Fig. 2(a), more extra active switches mean more losses and cost.

In order to decrease the root mean square (rms) current and save the number of active switches in traditional EET-DCX, this research paper first proposes the resonant commutation (RC) EET-DCX as shown in Fig. 1(b). The four switches in a typical EET unit are simplified as only one LV bidirectional switch. Moreover, the corresponding modulation is also developed for RC EET-DCX with a quasi-trapezoidal current. As shown in Fig. 1(b), the transformer current commutation from "positive" to "negative" utilizes a resonance between device paralleled capacitor and transformer leakage inductance L_k. Compared with triangular current and sinusoidal current in typical EET-DCX and CLLC-DCX, the rms current can be reduced up to 15% and 11%, respectively. By employing this resonant modulation technique, the quasi-trapezoidal current exhibits smaller rms and peak values under the same power transfer conditions. Benefiting from the proposed RC EET-DCX and corresponding current modulation, both total conduction losses and switching losses due to the lower rms current, peak current, and less active switch number. Notably, monolithic bidirectional switch [21]-[23] is undergoing a rapid development, which can further reduce the total losses and cost. Importantly, all the advantages associated with the typical EET-DCX presented in [1], such as natural current sharing, and load-independent voltage gain are retained in this proposed RC EET-DCX. It is worth noting that the magnetizing inductance is disregarded in this context as it exclusively pertains to the HV bridges' ZVS and is unrelated to the LV bridge's ZVS. Further details regarding the ZVS implementation of the HV bridges can be found in [1].

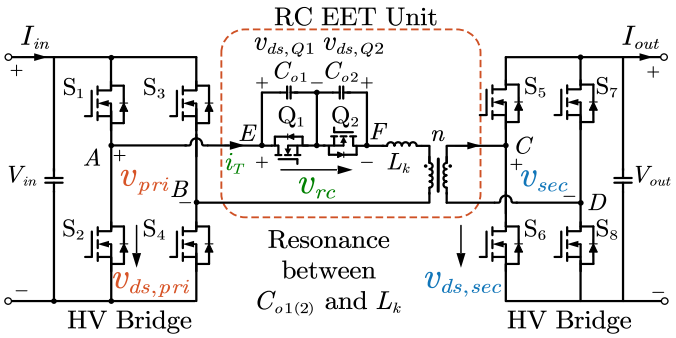

Fig. 2 Circuit diagram of the proposed RC EET-DCX.

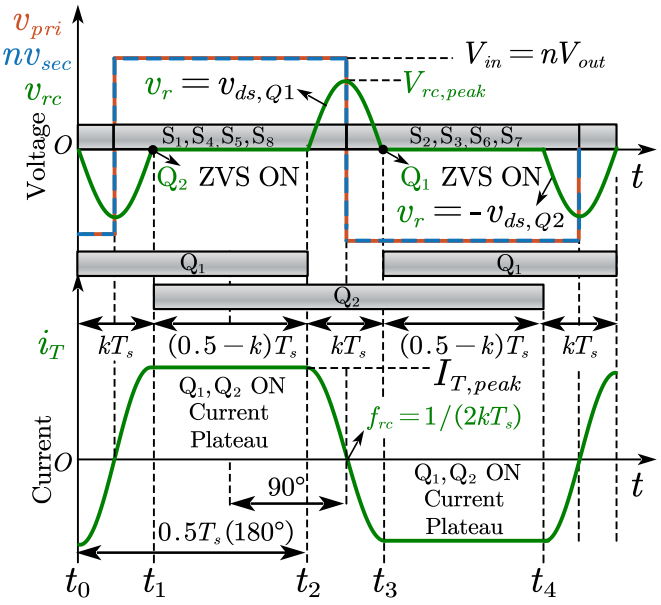

Fig. 3 Voltage and current waveforms of the proposed RC EET-DCX.

The paper is organized as follows. Section II proposes the concept of RC EET-DCX, and the operation principle of the corresponding quasi-trapezoidal current modulation. And then, to scale up the rating power, the natural current sharing mechanism among multiple paralleled RC EETs is explained in Section III. Finally, in Section IV, the proposed concept of RC EET and its corresponding merits are verified by a 12 kW RC EET-DCX prototype with four RC EET units in parallel.

II. Proposed RC EET-DCX

A. Operation Principle of RC EET-DCX

To better understand the proposed RC EET-DCX and its associated quasi-trapezoidal current modulation, the complete circuit diagram of RC EET-DCX is depicted in Fig. 2. And its corresponding voltages and currents waveforms are shown in Fig. 3. The transformer turns ratio is denoted as n and i_T represents the current flowing through the primary. V_{in} and V_{out} refer to the input and output voltages respectively, while v_{pri} and v_{sec} represent the HV bridge output voltages on the primary and secondary sides. Contrasting with the conventional EET-DCX [1], the entire LV bridge displayed in Fig. 1(a) is substituted with only one bidirectional ac switch $Q_{1(2)}$. C_{o1} and C_{o2} are two symmetric parallel capacitors.

$$C_{o1} = C_{o2} \tag{1}$$

Depending on the practical application, C_{o1} and C_{o2} can be the device's inherent parasitic capacitors or externally added components. $v_{ds,Q1}$ and $v_{ds,Q2}$ are two drain-to-source voltages across Q_1 and Q_2. v_{rc} is the output resonant voltage across point E and F, and its peak value is $v_{rc,peak}$ as shown in Fig. 3.

$$v_{rc} = Q_1 \cdot v_{ds,Q1} - Q_2 \cdot v_{ds,Q2} \quad (Q_{1(2)} = 0 \text{ OFF}/1 \text{ ON}) \tag{2}$$

L_k stands for the leakage inductances of the transformer. Following the conclusion from the conventional EET-DCX in [1], in the steady state, the relationship between V_{in} and V_{out}, I_{in} and I_{out}, as well as v_{pri} and v_{sec} can be initially defined in Eq. (3). The detailed explanation for this robust load-independent voltage gain will be discussed in this *Section II Part B*.

$$\begin{cases} V_{in} = n \cdot V_{out} \\ I_{in} = I_{out}/n \\ v_{pri} = n \cdot v_{sec} \end{cases} \tag{3}$$

As shown in Fig. 4, both HV bridges have the same driving signals, which ensures v_{pri} is in phase of v_{sec}. Moreover, the gate signals for Q_1 and Q_2 both have a duty cycle of (1-k), and they exhibit a 180-degree (half cycle) phase shift, as shown in Fig. 4. Compared to the HV bridge control signals, $Q_{1(2)}$ leads with a 90-degree phase shift from S_1, S_4, S_5, S_8 (S_2, S_3, S_6, S_7). Based on this driving logic and Eq. (3), it can be observed that when v_{pri} equals nv_{sec}, only the voltage v_{rc} will be utilized to drive L_k, resulting in the generation of a quasi-trapezoidal current waveform as shown in Fig. 4. In a half cycle (from t_0 to t_2), during the current commutation from t_0 to t_1 (kT_s), only switch Q_1 is ON, and C_{o2} will resonate with L_k at the frequency f_{rc}.

$$f_{rc} = \frac{1}{2\pi\sqrt{L_k C_{o1(2)}}} \tag{4}$$

If L_k and $C_{o1(2)}$ are designed to resonate for a half cycle during kT_s, an additional relationship between f_{rc} and f_s can be given as

$$f_{rc} = \frac{1}{2k} \cdot f_s \quad k \in (0, 0.5] \tag{5}$$

If the resonant frequency f_{rc} can be designed using Eq. (4) and (5), this half-cycle resonance between $C_{o1(2)}$ and L_k can be employed to realize the transformer current commutation during t_0-t_1 or t_2-t_3 as shown in Fig. 3. During the "Current Plateau" period from t_1 to t_2 ((0.5-k)T_s), both Q_1 and Q_2 are ON, making v_{rc} equal to 0. Due to no voltage across L_k, transformer current i_T remains flat as shown in Fig. 3. Moreover, the ZVS turn-on for Q_2 and Q_1 will be achieved at the end of resonance (t_1 or t_3) because $v_{ds,Q2}$ and $v_{ds,Q1}$ will drop to zero. This significantly differentiates from the conventional EET-DCX, which requires a full bridge to accomplish the current commutation. The complete RC EET-DCX current commutation only requires a single bidirectional ac switch Q_{12}.

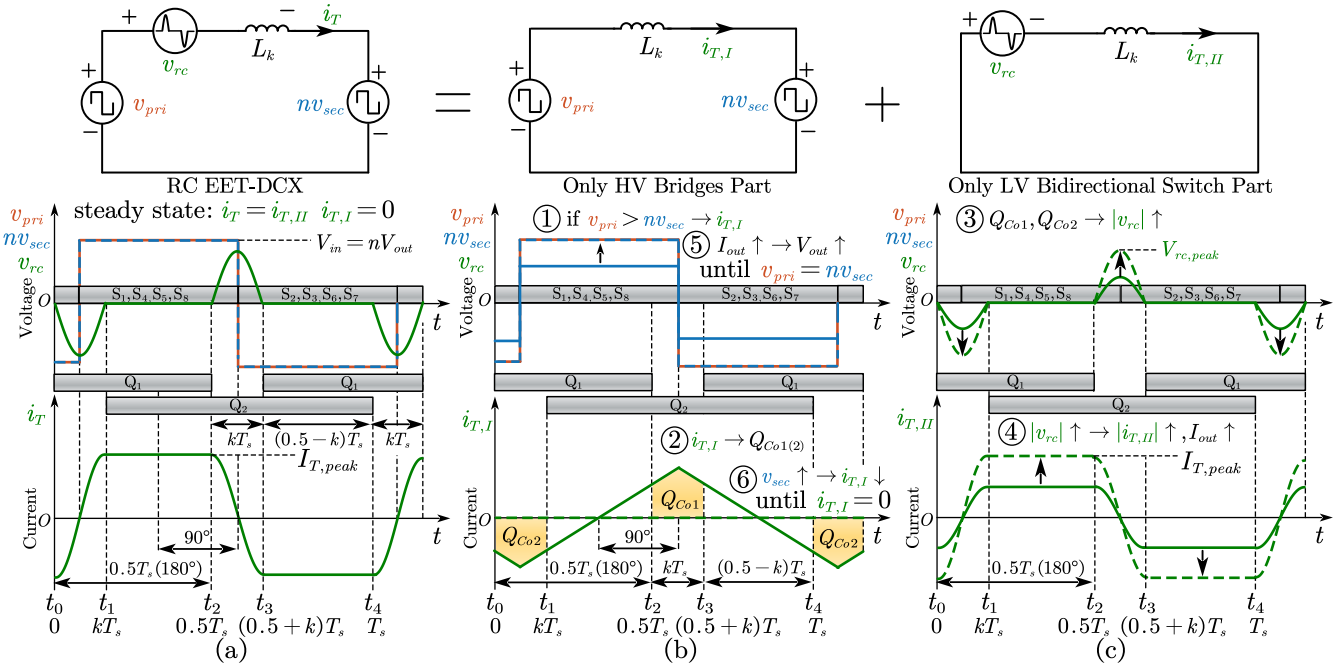

Fig. 4 Whole procedure of the robust load-independent voltage gain: (a) whole RC EET-DCX (b) only HV bridge part, and (c) only LV bridge part.

B. Robust Load Independent Voltage Gain

To illustrate the robust independent voltage gain of RC EET-DCX in Eq. (3), Fig. 4 shows the whole procedure with a certain load. Utilizing the superposition principle, RC EET-DCX shown in Fig. 4(a) can be disassembled into two components. The first is the HV bridges part shown in Fig. 4(b), while the second is LV bidirectional switch part depicted in Fig. 4(c). The operation principle of the robust load-independent voltage gain can be explained as six steps:

***Step* 1:** Assuming V_{in} is larger than nV_{out} as shown in Fig. 4(b), the voltage difference (V_{in}-nV_{out}) will be applied to L_k directly, causing the triangular current $i_{T,I}$ to exhibit a 90-degree phase shift from v_{pri} or v_{sec}. Obviously, due to this 90-degree phase shift, there is no real power delivered to the receiving side by $i_{T,I}$.

***Step* 2:** Since the current $i_{T,I}$ in Fig. 4(b) is in phase with the voltage v_C in Fig. 4(c), it will always charge the capacitors C_{o1} and C_{o2} alternately. For example, from t_0 to t_1, the current $i_{T,I}$ remains negative as shown in Fig. 4(b), and at the same time only LV switches Q_1 is ON (Q_2 is OFF). Therefore, the electric charge Q_{Co2} will be charged to C_{o2}. As for another half period from t_2 to t_3, positive $i_{T,I}$ will generate Q_{Co1} to charge the capacitor C_{o1}. In conclusion, over a complete cycle, Q_{Co1} equals to Q_{Co2} maintaining the waveform v_{rc} in a state of positive and negative symmetry.

***Step* 3:** If V_{in} is larger than V_{out}, Q_{Co1} and Q_{Co2} generated from current $i_{T,I}$ will always increase the amplitude of v_{rc} during the whole period.

$$i_{T,I} \rightarrow Q_{Co1}, Q_{Co2} \rightarrow |v_{rc}| \uparrow \tag{6}$$

***Step* 4:** As depicted in Fig. 4(c), when excited soley by the voltage source v_{rc}, the current $i_{T,II}$ assumes a quasi-trapezoidal shape and can be derived as

$$i_{T,II}(t) = \begin{cases} -I_{T,peak} \cdot \cos(2\pi f_{rc} \cdot t) & t \in [0,\ kT_s] \\ I_{T,peak} & t \in [kT_s,\ 0.5T_s] \end{cases} \tag{7}$$

where $I_{T,peak}$ represents the peak value of i_T, and the range of k is from 0 to 0.5. As the value of v_{rc} from Eq. (6) increases, the amplitude of the current $i_{T,II}$ will become larger as shown in Fig. 4(c). Additionally, the power $P_{T,II}$ delivered to the receiving side by $i_{T,II}$ can be given as

$$P_{T,II} = \int_0^{T_s} n \cdot v_{sec}(t) \cdot i_{T,II}(t) \tag{8}$$

Since v_{sec} is always in phase with $i_{T,II}$, with a larger $i_{T,II}$ shown in dash line, more real power $P_{T,II}$ will be delivered to the receiving side.

***Step* 5:** If the receiving power increases with a certain load, the corresponding output voltage V_{out} will increase until nV_{out} is equal to V_{in}.

$$I_{out} \uparrow \rightarrow V_{out} \uparrow, |v_{sec}| \uparrow \text{ until } n \cdot V_{out} = V_{in} \tag{9}$$

***Step* 6:** Meanwhile, assuming V_{in} is constant, an increasing V_{out} will lead to a smaller current $i_{T,I}$ until nV_{out} is equal to V_{in}.

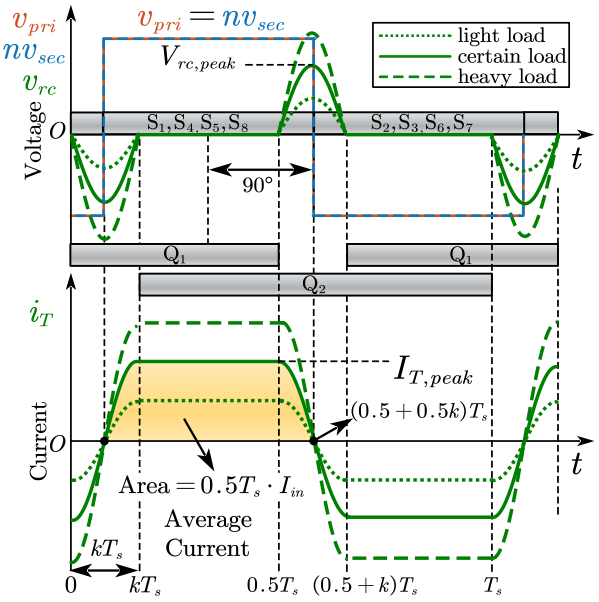

Fig. 5 Steady state waveforms of RC EET-DCX under different loads.

In summary, the whole mechanism of RC EET-DCX in Fig. 4 can be expressed as Eq. (10). When nV_{out} equals V_{in}, the current $i_{T,I}$ becomes zero and the peak voltage and current values, $V_{rc,peak}$ $I_{T,peak}$, respectively, remain constant, signifying that the RC EET-DCX has entered the steady state. Previous analysis from ***Step* 1-6** is based on the premise that V_{in} is larger than nV_{out}. Conversely, if V_{in} is smaller than nV_{out}, a similar analysis from Eq. (5)-(9) leads to the conclusion that $i_{T,II}$ will discharge capacitors C_{o1}, C_{o2} during t_0-t_1 and t_2-t_3 alternately, which will result in a reduction in the output current I_{out}. With a certain load, a reduced I_{out} will decrease V_{out} until V_{in} equals nV_{out}.

$$\begin{cases} V_{in} > nV_{out} & i_{T,II} \rightarrow |v_{rc}| \uparrow \rightarrow I_{out} \uparrow \rightarrow V_{out} \uparrow \\ V_{in} = nV_{out} & i_{T,II} = 0 \rightarrow \text{const } V_{rc,peak}, I_{T,peak},\ I_{out},\ V_{out} \\ V_{in} < nV_{out} & i_{T,II} \rightarrow |v_{rc}| \downarrow \rightarrow I_{out} \downarrow \rightarrow V_{out} \downarrow \end{cases} \tag{10}$$

C. Steady State of RC EET-DCX

In the steady state, with a turns ratio n, the input voltage V_{in} should be equal to nV_{out} based on the analysis in Eq. (10). Therefore, similar to the conventional EET-DCX [1], the proposed RC EET-DCX also maintains a robust, load-independent voltage gain as derived from Eq. (3).

As for the current i_T, the component $i_{T,I}$ should equate to 0 in the steady state. If not, this current will continue generate Q_{Co1} and Q_{Co2} as shown in Fig. 4(b). Consequently, the current i_T in steady state should be equal to $i_{T,II}$. Since this steady state is a stable equilibrium point, no additional control is required.

$$\begin{cases} i_{T,I} = 0 \\ i_T = i_{T,II} \end{cases} \tag{11}$$

Fig. 5 illustrates the steady-state waveforms of RC EET-DCX under varying load conditions. In the steady state, the transformer current i_T is in phase with terminal voltages v_{pri} and

v_{sec}, making the transformer current dedicated to real power transfer. With different loads, the amplitude of the quasi-trapezoidal current i_T is regulated via v_{rc} as shown in Fig. 5. Since i_T equals to $i_{T,II}$ in the steady state, the time-domain expression of i_T(t) can be directly found in Eq. (7). On the other hand, input dc current I_{in} equals to the average value of current i_T.

$$I_{in} = \text{average current} = \frac{2}{T_s}\int_{0.5kT_s}^{(0.5+0.5k)T_s} i_T(t)\cdot dt \tag{12}$$

From Eq. (7) and (12), the relationship between $I_{T,peak}$ and I_{in} can be given as

$$I_{T,peak} = \frac{\pi}{4\cdot k + (1-2\cdot k)\cdot \pi}\cdot I_{in} \tag{13}$$

Following Eq. (7), (13), the transformer rms current $i_{T,rms}$ can also be derived as

$$\begin{aligned} I_{T,rms} &= \frac{1}{T_s}\sqrt{\int_0^{T_s} {i_T}^2(t)\,dt} \\ &= \frac{\sqrt{1-k}\cdot\pi}{(1-2\cdot k)\cdot\pi + 4\cdot k}\cdot I_{in} \end{aligned} \tag{14}$$

As for the resonant voltage v_{cr} in the steady state, the time-domain expression of v_{cr}(t) can be give as

$$v_{cr}(t) = \begin{cases} -V_{cr,peak}\cdot\sin(2\pi f_{rc}\cdot t) & t\in[0,\ kT_s] \\ 0 & t\in[kT_s,\ 0.5T_s] \end{cases} \tag{15}$$

where the peak voltage value $V_{cr,peak}$ can be derived as

$$\begin{aligned} V_{rc,peak} &= L_k\cdot\left.\frac{di_T(t)}{dt}\right|_{t=(0.5+0.5k)T_s} \\ &= \frac{\pi^2}{k\cdot(4\cdot k+(1-2\cdot k)\cdot\pi)}\cdot f_s\cdot L_k\cdot I_{in} \end{aligned} \tag{16}$$

From Eq. (16), the peak voltage $V_{rc,peak}$ applied on the LV bidirectional switch Q_1 and Q_2 is proportional with switching frequency f_s, leakage inductance L_k, and input dc current I_{in}.

$$V_{rc,peak} \propto f_s,\ L_k,\ I_{in} \tag{17}$$

With a pre-determined I_{in}, f_s and k, minimizing the transformer leakage inductance L_k becomes crucial as it reduces the voltage stress on the LV bidirectional switch. By using a smaller voltage rating device, the bidirectional switch can be easily embedded into the high-frequency transformer windings. For instance, when I_{in} is 10 A, f_s is 200 kHz, k is 0.3, L_k is 300 nH, the voltage stress $V_{rc,peak}$ on bidirectional is only 8 V, as derived from (16). Importantly, the voltage stress $V_{rc,peak}$ is unrelated to input or output voltage $V_{in(out)}$ according to Eq. (16), indicating that this proposed RC EET-DCX can be adopted in high voltage applications. Therefore, even with large input and output voltages, an LV bidirectional switch can still be selected.

To summarize, since V_{in} is equal to nV_{out} at the steady state, the resonant voltage v_{rc} will be directly applied to L_k, compensating fully for the voltage drop on L_k with the embedded LV bidirectional switch.

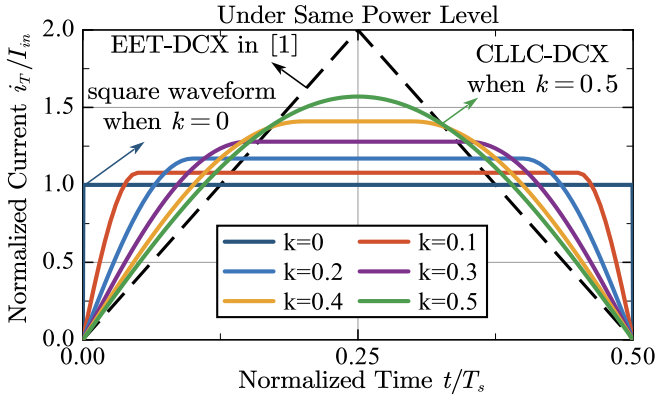

Fig. 6 RC EET-DCX normalized transformer current i_T/I_{in} with different k.

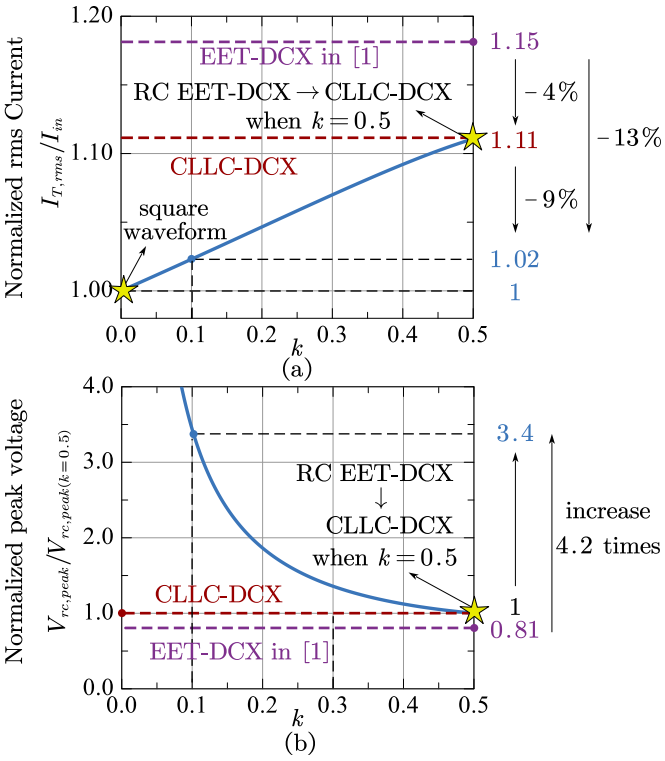

Fig. 7 Normalized current and voltage of the proposed RC EET-DCX: (a) normalized transformer rms current $I_{T,rms}$ based on input dc current I_{in}, (b) normalized peak voltage $V_{rc,peak}$ based on k=0.5 case. It should be noted that when k=0.5, proposed RC EET-DCX will be a traditional CLLC-DCX.

D. Comparison with LLC-DCX and typical EET-DCX in [1]

Based on the time-domain expression of $i_T(t)$ from Eq. (7), Fig. 6 illustrates the normalized transformer current i_T/I_{in} with different values of k. At the same power level, the current i_T is normalized based on the input dc current I_{in}. When $0 < k < 0.5$, the transformer current i_T exhibits a quasi-trapezoidal waveform composed of two parts: one represents the resonance part during current commutation, and the other part is the "current plateau". As k approaches 0, the current waveform changes to an ideal square waveform, while for k=0.5, the resonant current occupies the entire period, and the "current

plateau" disappears, effectively transitioning the RC EET-DCX to the traditional resonant CLLC-DCX. Additionally, for comparison purposes, the triangular current from a typical EET-DCX in [1] is depicted as a dashed line, assuming the same power rating.

Following Eq. (14), Fig. 7(a) depicts the normalized rms current $I_{T,rms}$ based on I_{in} for different values of k. In comparison with the sinusoidal current ($1.11 \cdot I_{in}$) observed in CLLC-DCX or k=0.5 case, the rms current can be reduced by 9% and 11% for k=0.1 and 0, respectively. Notably, for k=0.1, the rms current is significantly reduced by 13% compared to the typical EET-DCX in [1].

On the other hand, Fig. 7(b) represents the normalized peak voltage $V_{rc,peak}$ based on $V_{rc,peak}$ with k=0.5 from Eq. (16). The proposed RC EET-DCX and corresponding quasi-trapezoidal current modulation have one drawback: $V_{rc,peak}$ increases as k decreases. Theoretically, reducing k to 0 would yield a square waveform transformer current, which is optimal. However, based on Eq. (16), as k approaches 0, $V_{cr,peak}$ increases dramatically. For instance, when k=0.1, $V_{rc,peak}$ increases by 4.2 times compared to the typical EET-DCX in [1]. Therefore, there is a trade-off: as k approaches 0 and the quasi-trapezoidal current becomes more like a square waveform with a smaller rms current as shown in Fig. 6, it results in an increase in $V_{rc,peak}$ across the bidirectional switch as shown in Fig. 7(b). Nevertheless, in practical scenarios, $V_{rc,peak}$ is typically very small. For instance, when I_{in} is 10 A, f_s is 200 kHz, k is 0.1, L_k is 300 nH, the voltage stress $V_{rc,peak}$ on the bidirectional switch can be derived as only 20 V from (16). This indicates that the increased $V_{rc,peak}$ is acceptable when it leads to a reduction in rms current.

In conclusion, the proposed RC EET-DCX with its related quasi-trapezoidal current modulation offers several advantages. Firstly, it reduces the total number of devices from 4 (full bridge) to 2 (split) or 1 (monolithic). Additionally, the corresponding quasi-trapezoidal current can dramatically reduce the total conduction loss due to smaller rms current. It should be noted that the total conduction loss comprises two HV bridge power modules losses, one LV bidirectional switch's loss, and the transformer winding loss.

III. Transformer-level Parallel

A. Current Sharing Performance Overview

As mentioned in *Section I*, due to higher power density, the transformer-level parallel solution is more desirable than the converter-level parallel when the DCX rating power needs to be scaled up the. Fig. 8 depicts three transformer-level parallel solutions with CLLC, EET in [1], and proposed RC EET, respectively. Fig. 8(a) shows three detailed circuit diagrams: CLLC with a resonant capacitor, EET with a full bridge, and RC EET with a bidirectional switch. After transforming secondary parameters to the primary side, the corresponding simplified equivalent circuits are depicted in Fig. 8(b). $i_{T1\text{-}N}$ represents the transformer currents among each parallel unit, and $r_{w1\text{-}N}$ denotes the loop resistances on each parallel unit. Due to the robust, load independent voltage gain from Eq. (3), the two HV bridges in Fig. 8(a) are replaced by two identical square voltage sources v_{pri} and nv_{sec}. According to the topology solution, $v_{rc1\text{-}N}$ can be replaced by a sinewave (CLLC), a square wave (EET), or a combination of sinewave and zero-stage waveform (RC EET). Based on the Kirchoff's voltage law (KVL), the terminal voltage v_{AB} can be expressed as

$$V_{AB} = jwL_{kN} \cdot i_{TN} + v_{rcN} + r_{wN} \cdot i_{TN} \quad (N = 1, 2, 3 \ldots) \tag{18}$$

Since the current sharing performance of CLLC-DCX and EET-DCX has been illustrated in [1], the conclusions can be summarized as follows:

1) CLLC-DCX's current sharing performance is highly sensitive to the parameters, especially the tolerance on leakage inductance L_k. When the converter deviates from the resonant point, the current sharing becomes poor. Achieving precise current sharing in CLLC-DCX requires tight control over the parameters, which can be challenging during practical implementation.

2) EET-DCX proposed in [1] exhibits a very robust current sharing characteristic. This is because the square voltage source v_{rcN} always cancels out the impedance from the leakage inductance L_k. As a result, the current sharing is primarily determined by each parallel transformer's resistance r_w, which can be more easily controlled during the manufacturing or assembly processes.

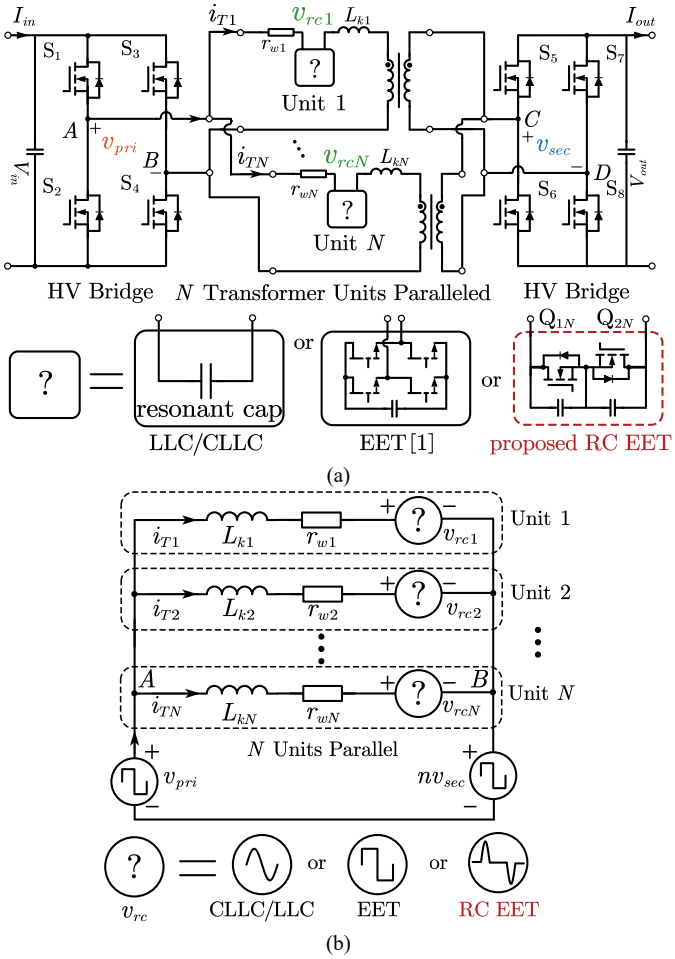

Fig. 8 Transformer-level parallel solution with LLC or EET or proposed RC EET unit: (a) circuit diagrams, (b) simplified equivalent circuits.

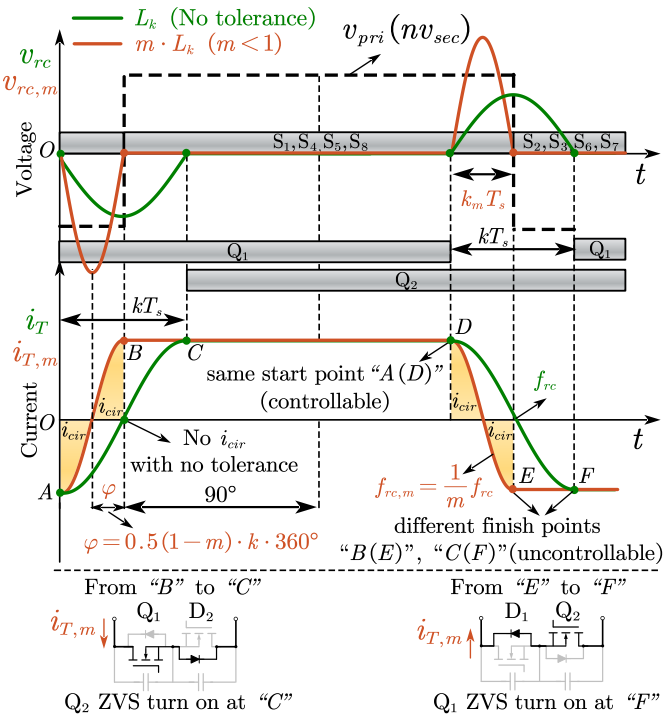

Fig. 9 Impact of the tolerance on leakage inductance L_k.

In Summary, the natural current sharing of EET-DCX is a result of a constant 90-degree phase shift between v_{rc} and $v_{pri(sec)}$. On the contrary, for resonant CLLC-DCX, v_{rc} will only have a 90-dgree phase shift from v_{rc} and $v_{pri(sec)}$ when it precisely operates at the resonant point. Deviations from this point can lead to significant challenges in achieving satisfactory current sharing.

B. Leakage Inductance Tolerance Impact

Regarding the proposed RC EET-DCX, the current sharing scenario differs from that of the typical EET-DCX due to the influence of the tolerance on L_k, which affects the resonant commutation frequency f_{rc} as per Eq. (4). To illustrate this impact, Fig. 9 demonstrates two cases: one with no tolerance and another when L_k has been multiplied by a factor m. Let's discuss the situation when m<1 first, implying that the real leakage inductance is smaller than the designed value L_k. In this case, with the tolerance factor m considered, both the resonant commutation voltage $v_{rc,m}$ and transformer current $i_{T,m}$ are plotted in Fig. 9.

As shown in Fig. 9, a smaller leakage inductance mL_k will results in an increased resonant commutation frequency from f_{rc} to $f_{rc,m}$. The relationship between $f_{rc,m}$ and the designed f_{rc} can be given as

$$f_{rc,m} = \frac{1}{m} \cdot f_{rc} \tag{19}$$

where f_{rc} can be easily derived from Eq. (4) and (5). According to the driving signals for bidirectional switches Q_1 and Q_2, the resonant current commutation in Fig. 9 will begin at the same time points "A" and "D", whether there is no tolerance (L_k) or with tolerance (mL_k). In the case of no tolerance, the entire current commutation will end precisely at points "C" and "F".

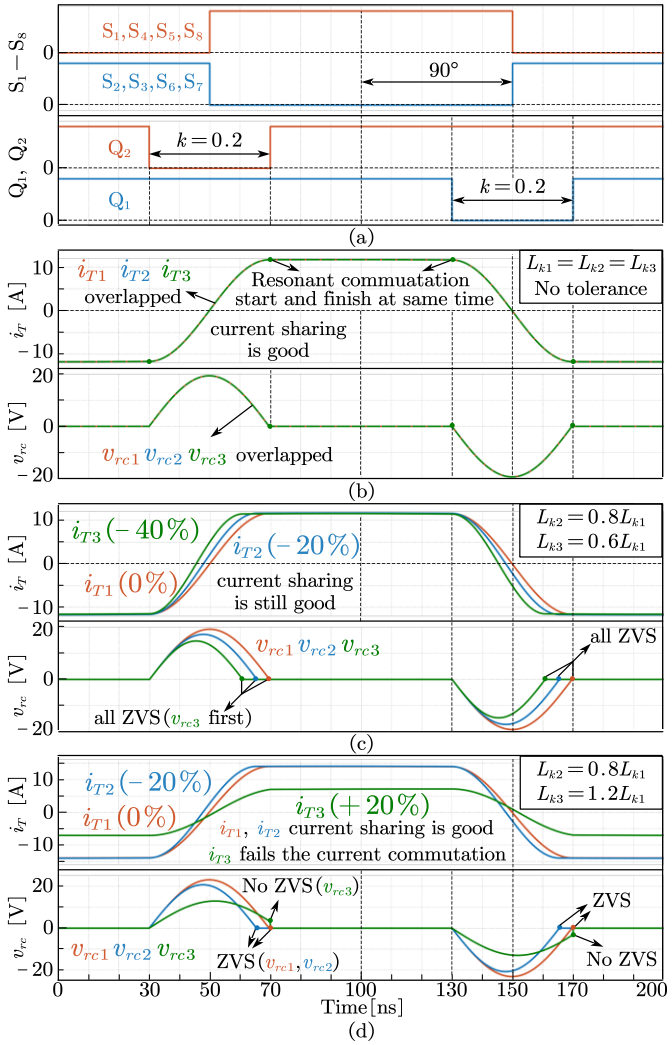

Fig. 10. Simulated currents and voltages of the proposed RC EET-DCX with the tolerance on leakage inductance.

TABLE I
CURRENT SHARING SIMULATION PARAMETERS

Variable	Value	Variable	Value
Input voltage V_{in}	300 V	Output voltage V_{out}	300 V
Parallel number N	3	Loop resistance r_w	100 mΩ
Rating power P	9 kW	Switching frequency f_s	500 kHz
Commutation index k	0.2	RC frequency f_{rc}	2.5 MHz
Leakage inductance L_k	210 nH	Parallel capacitance $C_{o1(2)}$	36.2 nF

At these two time points, bidirectional switches Q_2 and Q_1 will turn on to achieve the ZVS, respectively. On the other hand, in the case of tolerance with mL_k leakage inductance, the current commutation will end earlier at time points "B" and "E". After the current commutation, from "B" to "C" and "E" to "F", the transformer current $i_{T,m}$ will go through one device's channel Q_1 (Q_2) and another device's body diode D_2 (D_1) shown in Fig. 9. Even with the tolerance, bidirectional switches Q_1 and Q_2 can still achieve ZVS turn-on. The reason for this is that before these two devices turn on at points "C" and "F", the transformer current has already passed through their body diodes. Due to the tolerance, a small phase different between i_T and $i_{T,m}$ will occur, resulting in the existence of circulating current i_{cir}, as shown Fig. 9.

In conclusion, when the real leakage inductance is smaller than the design value, it can be considered equivalent to a new scenario with a small phase shift tolerance φ_m (defaulted to 90-dgree) and a new current commutation interval $k_m T_s$.

$$\varphi_m = 0.5 \cdot (1-m) \cdot k \cdot 360° \tag{20}$$

$$k_m = m \cdot k \tag{21}$$

Consider an example where k=0.2, and L_k has a -20% tolerance (m=0.8). In this case, the phase shift tolerance φ can be calculated as only 7.2 degree, and the new k_m is 0.16. Furthermore, the tolerance on phase shift itself, which is usually defaulted to 90-dgree, will be discussed in the next part of this section.

When the tolerance factor m is larger than 1, indicating that the real leakage inductance is larger than L_k, the bidirectional switches Q_1 and Q_2 will lose the ZVS, and the current sharing performance will be disrupted. This disruption occurs because the resonant current commutation cannot be completed within the time interval of kT_s. Fig. 10 illustrates the simulated waveforms of an RC EET-DCX with three transformers paralleled. The simulation parameters are provided in Table I. Fig. 10(a) shows the driving signals of HV bridges $S_{1\text{-}8}$ and LV bidirectional switches $Q_{1\text{-}2}$. In the case with no tolerance, depicted in Fig. 10(b), all three current overlap very well, and the current sharing is perfect.

Fig. 10(c) shows the case with m=0.8 (-20%) and m=0.6 (-40%) for L_{k2} and L_{k3}. Based on previous analysis in Fig. 9, although there is a small phase difference among three transformer currents i_{T1}, i_{T2}, and i_{T3} the current sharing remains good because the current commutation starts at the same point for these three cases.

Finally, the larger inductance case when m>1 is depicted in Fig. 10(d). As discussed earlier, when m>1, the current commutation fails, and LV bidirectional switches Q_1, Q_2 lose ZVS because the resonant commutation period becomes longer than kT_s. To ensure the resonant current commutation can be successfully completed, some margin on L_k needs to be considered in practical design cases. More details about the RC EET-DCX hardware design will be discussed in Section IV.

C. Phase Shift Tolerance Impact on Single Transformer

Since the tolerance on leakage inductance can be seen as a combination of phase shift tolerance and an adjusted k_m, the phase shift tolerance should be explained comprehensively. Firstly, with only one RC EET unit configuration (no parallel) as shown in Fig. 2, the phase shift tolerance impact is depicted in Fig. 11. Under ideal conditions, without any tolerance, the driving signals for HV bridges $S_{1\text{-}8}$ should maintain an open-loop 90-degree phase shift with the bidirectional switches $Q_{1\text{-}2}$. However, in real-world scenarios, small tolerance denoted by φ can arise due to gate drivers' propagation delay and other factors. As a result, the new gating signals $Q_{1(2),\varphi}$ are introduced in Fig. 11 to account for the phase shift tolerance. After considering this tolerance φ, the time domain expression for transformer current $i_{T,\varphi}(t)$ can be revised from Eq. (7).

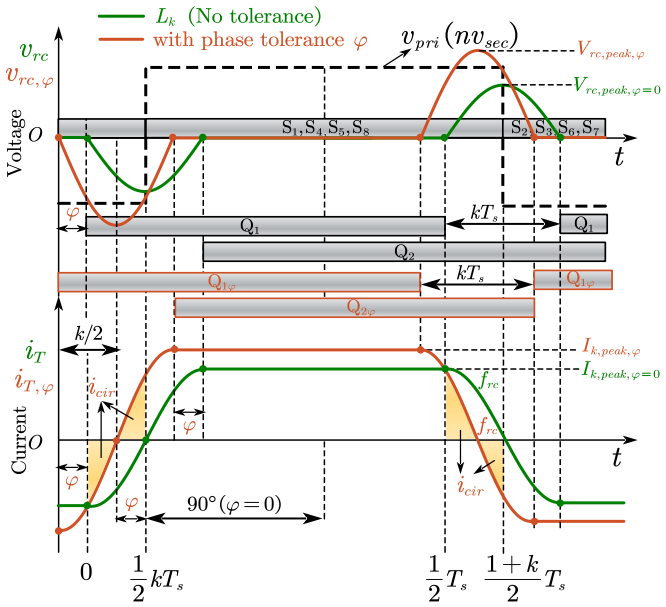

Fig. 11 Phase shift tolerance impact on single transformer RC EET-DCX.

$$i_{T,\varphi}(t) = \begin{cases} -I_{T,peak,\varphi} \cdot \cos(2\pi f_{rc} \cdot t + \varphi) & t \in [-\varphi,\ k-\varphi] \cdot T_s \\ I_{T,peak,\varphi} & t \in [k-\varphi,\ 0.5-\varphi] \cdot T_s \end{cases} \tag{22}$$

where $I_{T,peak,\varphi}$ is the peak value of the transformer current $i_{T,\varphi}$ with the tolerance. Similarly, the derivation of the $I_{T,peak,\varphi}$ in Fig. 11 can follow the average current calculation as below:

$$I_{in} = \text{average current} = \frac{2}{T_s}\int_{\frac{1}{2}kT_s}^{\frac{1+k}{2}T_s} i_{T,\varphi}(t) \cdot dt \tag{23}$$

From Eq. (22) and (23), the relationship between $I_{T,peak,\varphi}$ and I_{in} can be given as:

$$I_{T,peak,\varphi} = \frac{\pi}{(1-2k)\pi + 4k \cdot \cos\left(\frac{\varphi}{k} \cdot \pi\right)} \cdot I_{in} \tag{24}$$

Following the similar derivation in Section II, the corresponding peak resonant voltage value $V_{rc,peak,\varphi}$ and rms current $I_{T,rms,\varphi}$ can be both revised as

$$V_{rc,peak,\varphi} = \frac{\pi^2}{k \cdot \left((1-2k)\pi + 4k \cdot \cos\left(\frac{\varphi}{k}\pi\right)\right)} \cdot f_s L_k I_{in} \tag{25}$$

$$I_{T,rms,\varphi} = \frac{\sqrt{1-k} \cdot \pi}{(1-2k)\pi + 4k \cdot \cos\left(\frac{\varphi}{k}\pi\right)} \cdot I_{in} \tag{26}$$

From Eq. (26), with the phase shift tolerance φ from -18 degree to +18 degree, Fig. 12 depicts the normalized transformer current $I_{T,rms,\varphi}/I_{in}$ based on input dc current with different k. The black dash line in Fig. 12 shows the results with no tolerance (φ=0). When k=0.5, the RC EET-DCX transformer current will change from quasi-trapezoidal to pure sinusoidal current.

In conclusion, the tolerance on phase shift (defaulted to 90-degree) introduces a phase shift between terminal voltages $v_{pri(sec)}$ and transformer current $i_{T,\varphi}$ as shown in Fig. 12. As a

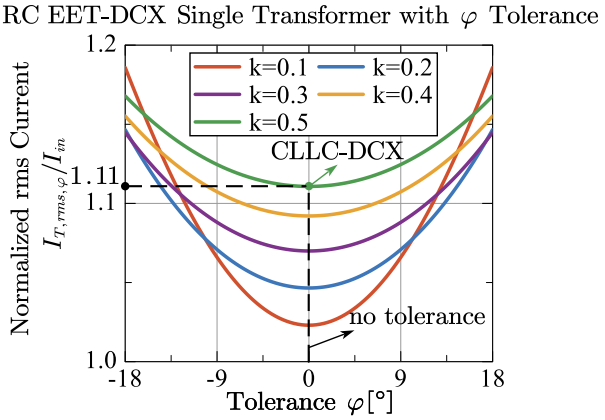

Fig. 12. Single transformer RC EET-DCX's normalized rms current with phase shift tolerance.

result, circulating currents and reactive power are induced in the system due to this phase shift tolerance φ. When transferring the same real power, the presence of reactive power caused by the phase shift tolerance φ leads to an increase in transformer rms current compared to the scenario with no tolerance, as shown in Fig. 12.

D. Phase Shift Tolerance Impact on Transformer Parallel

When multiple transformers are paralleled to scale up the rating power, the current sharing performance can be analyzed using the phasor diagram as shown in Fig. 13. In this diagram, the current i_{T1} branch represents no tolerance, while the current i_{T2} branch accounts for both L_k tolerance and phase shift tolerance. As discussed in this section *Part A*, φ_m represents the equivalent phase shift tolerance caused by L_k tolerance. Due to the application of the same driving signals to both the primary and secondary side HV bridges, v_{pri} is in phase with v_{sec}. However, in the load-independent analysis conducted in Section II, v_{pri} is considered equal to nv_{sec} since the voltage drop on winding resistance was neglected. In the current sharing analysis, this voltage cannot be ignored, leading to the existence of the voltage v_{AB}, which also shares the same phase with $v_{pri(sec)}$. Consequently, Eq. (18) can be converted into vector form.

$$\overrightarrow{v_{AB}} = \overrightarrow{i_{T1}} \cdot r_{w1} = \overrightarrow{i_{T2}} \cdot r_{w2} + \overrightarrow{v_{rc2}} - j\omega L_k \cdot \overrightarrow{i_{T2}} \tag{27}$$

From Eq. (27), it is evident that the branch i_{T1} (without tolerance) and branch i_{T2}(with tolerance) should have the same voltage drop v_{AB} as shown in Fig. 14. Based on this geometric relationship, the current sharing relationship between i_{T1} and i_{T2} can be expressed as

$$\overrightarrow{i_{T2}} \cdot r_{w2} = \overrightarrow{i_{T1}} \cdot r_{w1} \cdot \cos(\varphi + \varphi_m) \tag{28}$$

To generalize Eq. (28) for N transformer parallelled, the current sharing can be given by

$$i_{T1} : \cdots : i_{TN} = \frac{1}{r_{w1}\cos(\varphi_1 + \varphi_{m1})} : \cdots : \frac{1}{r_{w2}\cos(\varphi_N + \varphi_{mN})} \tag{29}$$

where φ_{mN} can be found in Eq. (20). In the steady state, the transformer unit without the tolerance will take more current,

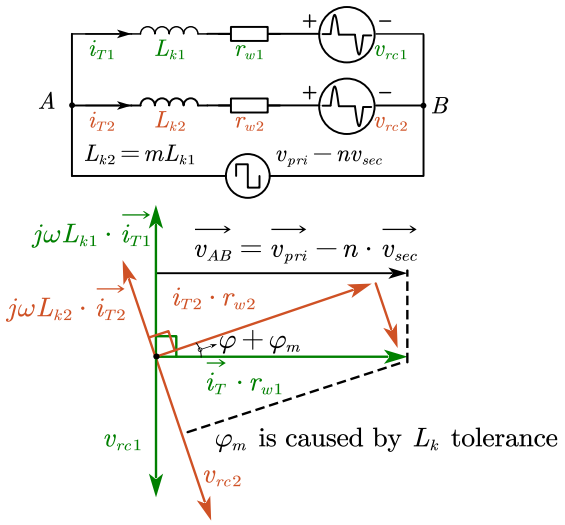

Fig. 13. Phasor diagram of the current sharing analysis with the phase shift tolerance.

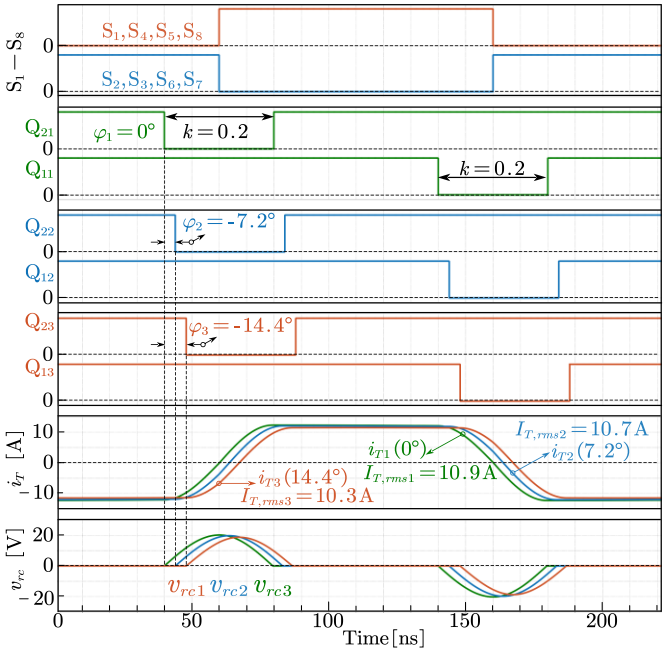

Fig. 14. Simulated current sharing results of the proposed RC EET-DCX with the tolerance on phase shift.

and the current sharing performance will be primarily determined by the total loop resistance r_w. The total loop resistance has a positive temperature coefficient and can be more easily controlled compared to inductance. Regarding the phase shift tolerance, for instance, if the phase difference is 14.4-degree, the current difference will be only 3%. With the same parameters listed in Table I, Fig. 14 displays the simulated current sharing results considering the phase shift tolerance. Among the three paralleled branches, i_{T1}, i_{T2}, and i_{T3}, the phase shift tolerance is 0, -7.2, and -14.4 degrees, respectively. As there is no tolerance on L_k, all three currents can complete the current commutation during kT_s. A small phase difference is observed among these three currents in Fig. 14. However, the rms current for i_{T1}, i_{T2}, and i_{T3} are 10.9, 10.7, and 10.3 A,

respectively, in accordance with the relationship from Eq. (29). In conclusion, the simulation results in Fig. 14 demonstrate a good current sharing RC EET-DCX even with phase shift tolerance. It should be noted that the phase shift tolerance will have a similar impact on the current sharing performance of the typical EET-DCX in [1].

IV. Hardware and Implementation

A. Hardware Design for two 12 kW DCXs

To verify the operation principle and advantages, two 12-kW DCX prototypes were built in this section, including the proposed RC EET-DCX and EET-DCX in [1]. As shown in Fig. 15(a), to achieve a fair comparison, both DCXs were based on one same platform, with two HV bridges shared between the two prototypes. To verify the current sharing performance, four RC EET/EET units are paralleled. As for the transformer part shown in Fig. 15(b), the proposed RC EET unit has the same size and the same winding layout as the typical EET unit in [1]. All the parameters of the proposed 12 kW RC EET-DCX are listed in Table II. For the typical EET-DCX, the bidirectional switches $Q_{1(2)}$ in RC EET unit are replaced by an LV full bridge. Both RC EET and EET unit adopted the same 80 V GaN device *EPC 2029*. Additionally, RC EET unit has sufficient space to accommodate measurement ports for $v_{ds,Q1}$ and $v_{ds,Q2}$, thanks to the reduced number of devices and drivers.

It's important to highlight that both of these 12 kW DCXs shared the same Silicon Carbide (SiC) based HV bridges on primary and secondary sides. The only distinction between the RC EET-DCX and the typical EET-DCX lies in the transformer unit part, as shown in Fig. 15(b). As the total rating power is 12 kW with four transformer units paralleled, each unit is individually designed for 3 kW (300 V, 10 A). Based on the parameters of L_k and C_{o1}, the ideal value of k can be calculated as 0.22 using Eq. (4) and (5). However, to prevent any potential current commutation failure caused by L_k tolerance, a small margin will be incorporated. As a result, k should be slightly larger than 0.22, ensuring stable and reliable operation.

B. RC EET-DCX

Fig. 16 presents the experimental results of the proposed RC EET-DCX under both full load (12 kW) and half load (6 kW) conditions. Considering a small margin left for k, the selected value is set to 0.26. In Fig. 16(a), the full load results display the split currents $i_{T1\text{-}4}$, with the drain-to-source voltage $v_{ds,Q1,T1}$ of Q_1 on Transformer unit T_1 representing the half cycle of voltage v_c. The current commutation from the "negative plateau" to the "positive plateau" is achieved through a half cycle resonance between L_k and C_{o1}. Similarly, the commutation from the "positive plateau" to the "negative plateau" is achieved through resonance between L_k and C_{o2} on the other half cycle. As the margin on on k is small, the entire commutation process finishes a little earlier than the bidirectional switch turning on, resulting in a small voltage drop on $v_{ds,Q1,T1}$ after the current commutation. The transformer current subsequently goes through the body diode of the bidirectional switch before achieving ZVS. Fig. 16(b) shows all four transformer currents from Fig. 16(a) overlapped together,

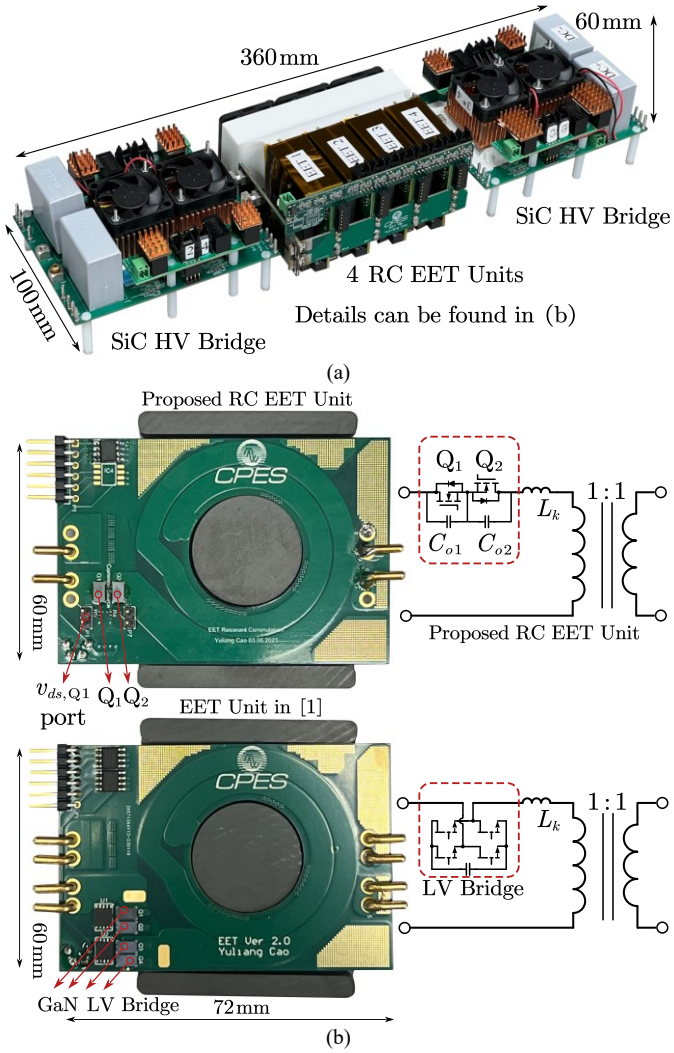

Fig. 15 A 12 kW DCX prototype with four configurable transformer units paralleled, (a) whole converter, (b) detailed design of the proposed RC EET unit and EET unit.

TABLE II
PARAMETERS OF RC EET-DCX WITH FOUR EET UNITS

Variable	Value	Variable	Value
$V_{in(out)}$	300 V	$C_{o1(2)}$	22.7 nF
P	12 kW	f_s	200 kHz
L_k	620 nH	$L_{pri(sec)}$	15 μH
ER Core	ECW64A18	Core Material	DMR51
$C_{oss,pri(sec)}$	418 pF × 2	$C_{oss,LV}$	1310 pF
HV Bridge	C3M0016120k × 2	LV Q_1 and Q_2	EPC 2029

demonstrating excellent matching and verifying the current sharing performance of the proposed RC EET-DCX.

Furthermore, Fig. 16(c) and (d) display the half load (6 kW) results. As expected, with reduced load, the amplitude of resonant voltage $v_{ds,Q1,T1}$ and all transformer currents $i_{T1\text{-}4}$ are halved, consistent with Eq. (13) and (16). These equations predict that the peak voltage of $v_{ds,Q1,T1}$ and peak current of $i_{T1\text{-}4}$ should be proportional to the input dc current I_{in}, leading to a halved value when transferring half the power.

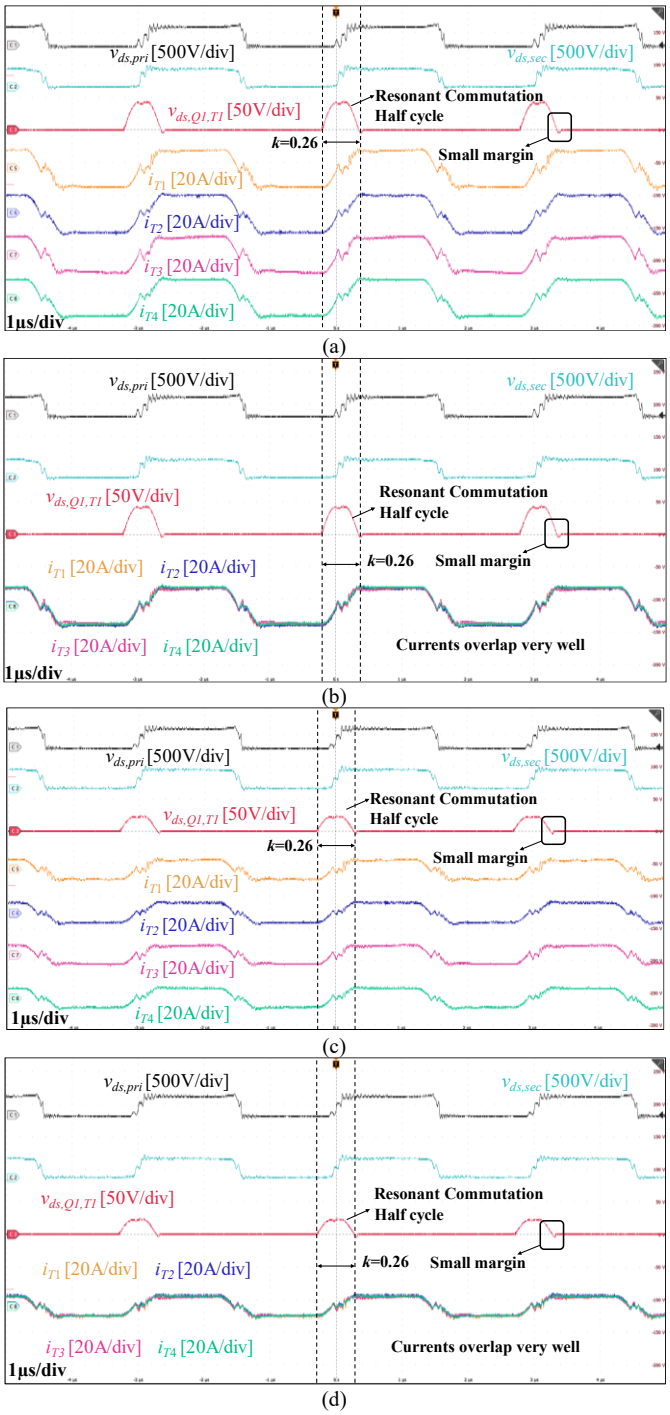

Fig. 16 The experimental results of RC EET-DCX with four paralleled transformers (k=0.26 to give a small margin for current commutation): (a) 12 kW full load with split current, (b) 12 kW full load with overlapped current, (c) 6 kW half load with split current, (d) 6 kW half load with overlapped current.

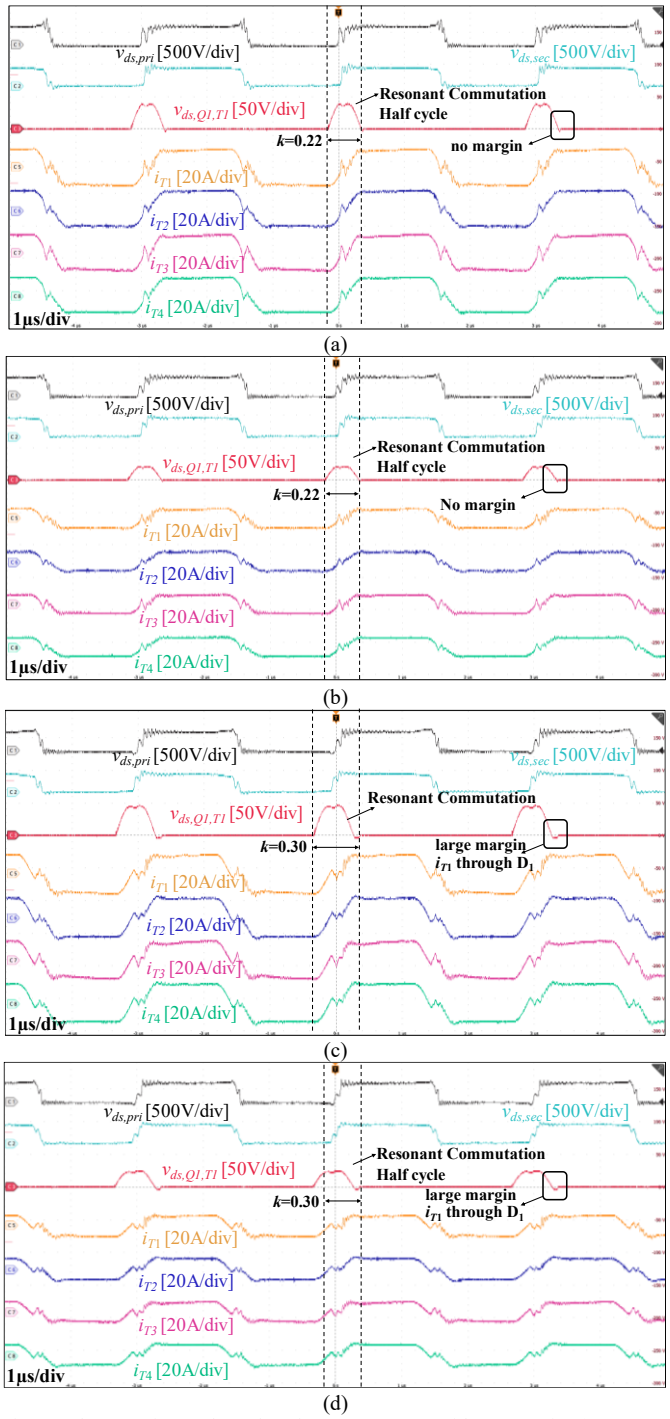

Fig. 17 The experimental results of RC EET-DCX with no margin (k=0.22) and large margin (k=0.30) design (a) 12 kW full load with no margin k=0.22, (b) 6 kW half load with no margin k=0.22, (c) 12 kW full load with large margin k=0.30, (d) 6 kW half load with large margin k=0.30.

Fig. 17 illustrates two additional cases with different k values. In Fig. 17(a) and (b), the "no margin" case has k=0.22. Under both full load and half load conditions, the resonant current commutation precisely finishes when the bidirectional LV switch turns on. As a result, no current passes through the body diodes of Q_1 or Q_2, and thus there is no voltage drop after the current commutation. However, this scenario is more sensitive to the L_k tolerance, as a larger L_k could cause the current commutation failure, leading to a loss of ZVS in bidirectional switches Q_1 and Q_2.

In contrast, Fig. 17(c) and (d) depict the "large margin" case with k=0.30. Compared to k=0.26 case in Fig. 16, a longer time for voltage drop is observed after the current commutation. This is due to the transformer current passing through the body diodes of Q_1 and Q_2 for a longer time.

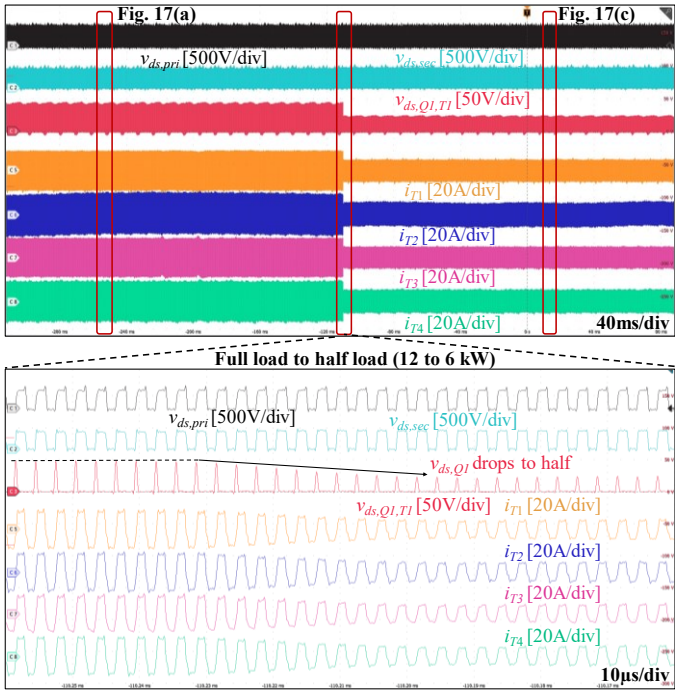

Fig. 18 Load changing test results of the proposed 12 kW RC EET-DCX from 12 kW full load to 6 kW half load.

To summarize, the selection of k involves a drade-off. A "no margin" approach (smallest k) offers efficiency benefits as no current passes through the body diodes. However, it becomes more sensitive to L_k tolerance, especially with a larger L_k values. In practice, a small margin is usually given, and the final selected k is slightly larger than the calculated value, depending on the actual tolerance situation.

Fig. 18 shows the load-changing test results with a smaller margin (k=0.26). The detailed steady state waveforms for full load and half load are found in Fig. 16(a) and (c), respectively, while the zoomed-in load transient waveforms are provided on the bottom. When the load suddenly changes from full load to half load, the amplitudes of the resonant voltage $v_{ds,Q1,T1}$ and all four currents gradually reduce to half in about 6 cycles. It's worth noting that the current sharing performance of the proposed RC EET-DCX remains good during the load transient period.

C. Typical EET-DCX

To ensure a fair comparison with the proposed RC EET-DCX, a 12-kW EET-DCX prototype was also built based on the transformer unit shown in Fig. 15(b). More details about the operation principle of the EET-DCX can be found in [1]. With an integrated LV full bridge, the current waveform for EET-DCX is triangle, as shown in Fig. 19.

Fig. 20(a) depicts the 12-kW full load split current results for the EET-DCX. Upon overlapping the four EET units, as shown in Fig. 20(b), the excellent current sharing performance can also be verified. However, in comparison to the quasi-trapezoidal current in the RC EET-DCX, the triangular current in the EET-DCX has a larger rms current, leading to higher total conduction loss. Additionally, despite achieving ZVS turn-on

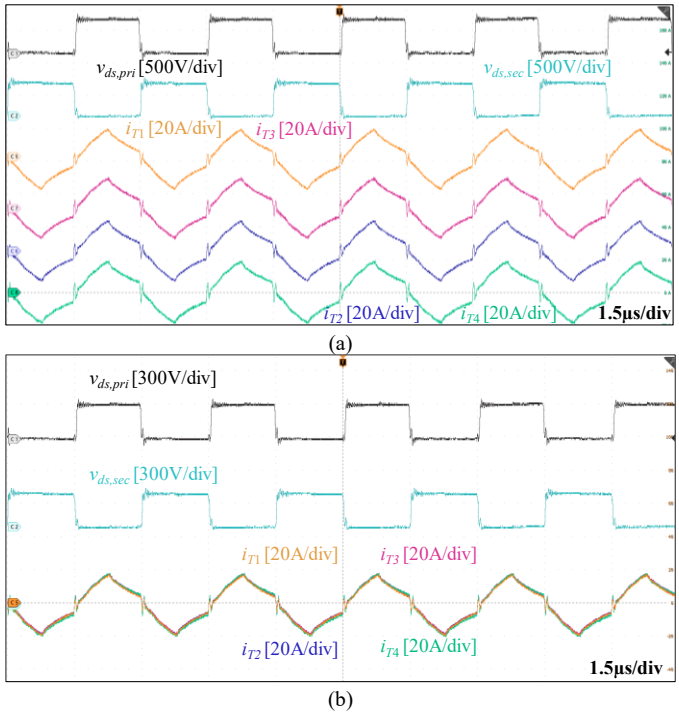

Fig. 19 The full load 12 kW experimental results of the typical EET-DCX with (a) split current, (b) overlapped current.

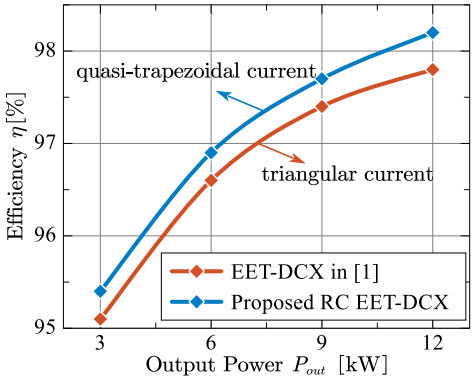

Fig. 20. The measured efficiency of *EET-DCX II* with different output power.

in both the RC EET-DCX and EET-DCX, the former also leads to smaller turn-off switching losses.

C. Efficiency Measurement

Fig. 20 shows the efficiency results for both the proposed RC EET-DCX and the typical EET-DCX. Based on previous analysis, the triangular current waveform in EET-DCX exhibits a higher rms current compared to the quasi-trapezoidal current in RC EET-DCX. It is crucial to emphasize that this reduction in conduction loss is not limited to just the transformer windings but also extends to encompass the conduction loss of the HV bridge devices. As a result, when compared to the typical EET-DCX, the proposed RC EET-DCX demonstrates higher overall efficiency (reaching 98.4% at 12 kW) across the entire load range. This efficiency advantage proves to be particularly beneficial in high-current, high-power applications, as the additional loss on the LV bridge becomes less significant in comparison.

V. Conclusion

This paper introduces a simplified topology RC EET-DCX with quasi-trapezoidal current. Compared to typical EET-DCX, the full bridge was replaced by only one bidirectional switch, and thus the device number was reduced by half. And then, the corresponding quasi-trapezoidal current modulation was developed for RC EET-DCX, which offers significant advantages such as a considerable reduction in rms current while preserving key features like natural current sharing, load-independent voltage gain, and full load range zero-voltage switching (ZVS). This conduction loss decrease enables a more compact transformer design. In addition, benefits from the inherent current sharing characteristic, the power rating of RC EET-DCX can be easily scaled up by modular transformers parallel.

Finally, the effectiveness of the proposed RC EET-DCX and quasi-trapezoidal current modulation technique are both validated through experimentation on a 12 kW RC EET-DCX prototype comprising four paralleled EET units. Under all load conditions, the proposed RC EET-DCX with trapezoidal current modulation exhibits higher efficiency than EET-DCX. This promising outcome demonstrates the significant potential to enhance the performance of DCX systems employed in high-power and high-density applications, such as electric vehicle charging systems and solid-state transformers.

References

[1] Y. Cao, K. D. T. Ngo and D. Dong, "A Scalable Electronic-Embedded Transformer (EET), a New Concept toward Ultra-high-frequency High-power Transformer in DC-DC Converters" in IEEE Transactions on Power Electronics, doi: 10.1109/TPEL.2023.3279259.

[2] D. Dong et al., "A PV Residential Microinverter with Grid-Support Function: Design, Implementation, and Field Testing," in IEEE Transactions on Industry Applications, vol. 54, no. 1, pp. 469-481, Jan.-Feb. 2018.

[3] F. Z. Peng, Hui Li, Gui-Jia Su and J. S. Lawler, "A new ZVS bidirectional DC-DC converter for fuel cell and battery application," in IEEE Transactions on Power Electronics, vol. 19, no. 1, pp. 54-65, Jan. 2004.

[4] Y. Cao, M. Ngo, N. Yan, D. Dong, R. Burgos and A. Ismail, "Design and Implementation of an 18 kW 500 kHz 98.8% Efficiency High-density Battery Charger with Partial Power Processing," in IEEE Journal of Emerging and Selected Topics in Power Electronics.

[5] F. Jin, A. Nabih, C. Chen, X. Chen, Q. Li and F. C. Lee, "A High Efficiency High Density DC/DC Converter for Battery Charger Applications," 2021 IEEE Applied Power Electronics Conference and Exposition (APEC), 2021, pp. 1767-1774.

[6] Y. Cao, M. Ngo, D. Dong and R. Burgos, "Bidirectional Architectures with Partial Energy Processing For DC/DC Converters," U.S. Patent 20220069719A1, Mar. 29, 2022.

[7] Y. Cao et al., "Design and Implementation of High-density Isolated Bi-directional Soft-switching Resonant DC-DC Converter with Partial Power Processing," 2021 IEEE Applied Power Electronics Conference and Exposition (APEC), 2021, pp. 640-646.

[8] B. Li, Q. Li, F. C. Lee, Z. Liu and Y. Yang, "A High-Efficiency High-Density Wide-Bandgap Device-Based Bidirectional On-Board Charger," in IEEE Journal of Emerging and Selected Topics in Power Electronics, vol. 6, no. 3, pp. 1627-1636, Sept. 201.

[9] M. Ngo, Y. Cao, D. Dong and R. Burgos, "Design of 500 kHz, 18 kW Low Leakage Inductance Intraleaved Litz Wire Transformer for Bi-directional Resonant DC-DC Converter," 2021 IEEE Applied Power Electronics Conference and Exposition (APEC), 2021, pp. 1153-1161.

[10] J. A. Ferreira, "Improved analytical modeling of conductive losses in magnetic components," in IEEE Transactions on Power Electronics, vol. 9, no. 1, pp. 127-131, Jan. 1994.

[11] D. Dong, M. Agamy, J. Z. Bebic, Q. Chen and G. Mandrusiak, "A Modular SiC High-Frequency Solid-State Transformer for Medium-Voltage Applications: Design, Implementation, and Testing," in IEEE Journal of Emerging and Selected Topics in Power Electronics, vol. 7, no. 2, pp. 768-778, June 2019.

[12] Z. Li, Y. -H. Hsieh, Q. Li, F. C. Lee and M. H. Ahmed, "High-Frequency Transformer Design with High-Voltage Insulation for Modular Power Conversion from Medium-Voltage AC to 400-V DC," 2020 IEEE Energy Conversion Congress and Exposition (ECCE), 2020, pp. 5053-5060.

[13] C. Zhao, Y. -H. Hsieh, F. C. Lee and Q. Li, "Design and Analysis of a High-frequency CLLC Resonant Converter with Medium Voltage insulation for Solid-State-Transformer," 2021 IEEE Applied Power Electronics Conference and Exposition (APEC), 2021, pp. 1638-1642.

[14] Y. Cao, M. Ngo, N. Yan, Y. Bai, R. Burgos and D. Dong, "DC Distribution Converter with Partial Power Processing for LVDC/MVDC Systems," 2021 IEEE Fourth International Conference on DC Microgrids (ICDCM), 2021, pp. 1-8.

[15] B. Li, Q. Li and F. C. Lee, "High-Frequency PCB Winding Transformer with Integrated Inductors for a Bi-Directional Resonant Converter," in IEEE Transactions on Power Electronics, vol. 34, no. 7, pp. 6123-6135, July 2019.

[16] B. Zhao, Q. Song, W. Liu and Y. Sun, "Overview of Dual-Active-Bridge Isolated Bidirectional DC–DC Converter for High-Frequency-Link Power-Conversion System," in IEEE Transactions on Power Electronics, vol. 29, no. 8, pp. 4091-4106, Aug. 2014.

[17] Y. Cao, M. Ngo, R. Burgos, A. Ismail and D. Dong, "Switching Transition Analysis and Optimization for Bidirectional CLLC Resonant DC Transformer," in IEEE Transactions on Power Electronics, vol. 37, no. 4, pp. 3786-3800, April 2022.

[18] Y. Cao, M. Ngo, D. Dong and R. Burgos, "A Simplified Time-Domain Gain Model for CLLC Resonant Converter," 2021 IEEE Energy Conversion Congress and Exposition (ECCE), 2021, pp. 3079-3086.

[19] T. Guillod, D. Rothmund, and J. W. Kolar, "Active Magnetizing Current Splitting ZVS Modulation of a 7 kV/400 V DC Transformer," IEEE Trans. Power Electron., vol. 35, no. 2, pp. 1293–1305, Feb. 2020.

[20] Y. Cao, M. Ngo, D. Dong and R. Burgos, "The ZVS Transition Analysis and Optimization for CLLC-Type Resonant DC Transformer," 2021 IEEE Energy Conversion Congress and Exposition (ECCE), 2021, pp. 3126-3133.

[21] V. Veliadis, "Monolithic Bidirectional WBG Switches Rekindle Power Electronics Technology [Expert View]," in IEEE Power Electronics Magazine, vol. 10, no. 1, pp. 71-75, March 2023, doi: 10.1109/MPEL.2023.3235466.

[22] J. Huber and J. W. Kolar, "Monolithic Bidirectional Power Transistors," in IEEE Power Electronics Magazine, vol. 10, no. 1, pp. 28-38, March 2023, doi: 10.1109/MPEL.2023.3234747.

[23] B. J. Baliga et al., "The BiDFET Device and Its Impact on Converters," in IEEE Power Electronics Magazine, vol. 10, no. 1, pp. 20-27, March 2023, doi: 10.1109/MPEL.2023.3237059.